Effect of turbulence and viscosity models on wall shear stress derived biomarkers for aorta simulations

Antonio Martinez-Sanchez, Martijn Hoeijmakers, Leonardo Geronzi, Valéry Morgenthaler, Jacques Tomasi, Michel Rochette, Marco E. Biancolini

Effect of Turbulence and Viscosity Models on Wall Shear Stress Derived Biomarkers for Aorta Simulations

Antonio Martínez[a,b], Martijn Hoeijmakers[c], Leonardo Geronzi[a,b], Valery Morgenthaler[b], Jacques Tomasi[d], Michel Rochette[b] and Marco E. Biancolini[a]

[a] University of Rome Tor Vergata, Rome, Italy
[b] Ansys France, Villeurbanne, France
[c] Ansys Netherlands, Zoetermeer, Netherlands
[d] University of Rennes, CHU Rennes, Inserm, LTSI-UMR 1099, F-35000, Rennes, France

ARTICLE INFO

Keywords:
Ascending aorta
Wall shear stress
Viscosity
Non-Newtonian
Turbulence model
Dynamic Smagorinsky-Lilly
LES

ABSTRACT

Ascending aorta simulations provide insight into patient-specific hemodynamic conditions. Numerous studies have assessed fluid biomarkers which show a potential to aid clinicians in the diagnosis process. Unfortunately, there exists a large disparity in the computational methodology used to model turbulence and viscosity. Recognising this disparity, some authors focused on analyzing the influence of either the turbulence or viscosity models on the biomarkers in order to quantify the importance of these model choices. However, no analysis has yet been done on their combined effect. In order to fully understand and quantify the effect of the computational methodology, an assessment of the combined effect of turbulence and viscosity model choice was performed. Our results show that (1) non-Newtonian viscosity has greater impact (2.9-5.0%) on wall shear stress than Large Eddy Simulation turbulence modelling (0.1-1.4%), (2) the contribution of non-Newtonian viscosity is amplified when combined with a subgrid-scale turbulence model, (3) wall shear stress is underestimated when considering Newtonian viscosity by 2.9-5.0% and (4) cycle-to-cycle variability can impact the results as much as the numerical model if insufficient cycles are performed. These results demonstrate that, when assessing the effect of computational methodologies, the resultant combined effect of the different modeling assumptions differs from the aggregated effect of the isolated modifications. Accurate aortic flow modeling requires non-Newtonian viscosity and Large Eddy Simulation turbulence modeling.

1. Introduction

Computational biomarkers are emerging as a tool to aid in the diagnosis process of cardiovascular diseases. Their capability to provide insight into patient-specific hemodynamic and wall conditions position them as a promising tool that will enable clinicians to provide personalized treatment. For decades, numerical models of the cardiovascular system have been developed with varying levels of personalization and complexity (1; 2; 3). In order to take in-silico model into the healthcare industry, standardized methodologies will be required to obtain approval by the corresponding regulatory agency through a process of validation and verification of the model outputs, ensuring trustworthy and replicable results (4; 5).

Computational Fluid Dynamics (CFD) and Fluid-Structure Interaction (FSI) models have been extensively used to evaluate pathological ascending thoracic aortas (ATA) by quantifying clinically-relevant hemodynamic biomarkers related to aneurysm (6; 7; 8; 9) and dissection (10; 11; 12) progression. Some studies have been performed considering Newtonian viscosity (NV) and the absence of turbulence models (6; 8), while others have considered a non-Newtonian viscosity and Large Eddy Simulation (LES) turbulence models, which require higher computational effort (13; 14; 15).

martinez@ing.uniroma2.it (A. Martínez)

We also find studies that consider only the non-Newtonian behaviour in the absence of turbulence models (16; 17) or, on the contrary, consider a turbulence subgrid model with constant viscosity (7; 18).

Blood is a non-Newtonian fluid with a shear-thinning behaviour which reaches a Newtonian plateau at high shear rates (19). The rheological response is primarily modulated hematocrit (20). It is argued that, under the high shear-rates present in the ascending aorta during the most part of the cardiac cycle, the variations in viscosity are negligible and therefore a NV model can be assumed. A thorough assessment on the influence of viscosity models on aortic valves and ATA simulations have shown otherwise and revealed higher wall shear stress (WSS) and increased hemolysis when accounting for non-NV (21; 22). Moreover, shear-thinning has a significant effect on the growth of vortical structures and recirculation zones on idealized curved vessels (23) and has shown to delay turbulent transition on straight pipe flows (24; 25; 26). Other studies have analyzed the flow through stenosed arteries considering NV and non-NV (27; 28). Pathologies such as valve stenosis or the presence of a bicuspid aortic valve favour turbulence generation as the aortic valve area is reduce and the jet velocity increased (29; 30).

The effect of turbulence model choice has been assessed for various ATA under different scenarios, in order to clarify the computational requirements of different biomarkers. High and low resolution laminar models have been compared against Wall-Adapting Local Eddy-Viscosity (WALE) subgrid-scale model using constant viscosity and it was shown that high resolution laminar models were capable of capturing accurately shear and turbulence dynamics, but had equal computational cost as LES simulation (31). Variations in spatially and time averaged WSS have revealed differences below 6% between laminar and WALE considering a Carreau viscosity model (32). The effect of turbulence modelling on platelet activation was assessed by comparing laminar, RANS, LES and Direct Numerical Simulation (DNS), revealing that predicting blood cell damage required LES or DNS and that RANS, due to its inherent temporal filtering nature, should be avoided as it shortens particle trajectories and alters the shear stress over the platelets (33). In (13) it was shown that the $k-\omega$ SST model significantly underestimated the turbulent kinetic energy and anisotropy levels when compared to the WALE model under non-Newtonian viscosity. Differences between different LES models and their sensitivity to grid size and convection schemes have been analyzed in (34).

When considering non-NV, we should also emphasise that the shear-thinning behaviour can be described using different models, such as Carreau, Casson and Power-law. The choice made will also influence the flow behaviour, as shown in (35), where an ATA was modeled considering ten viscosity models and the results compared in terms of velocity and WSS.

To our knowledge, only one study (36) has addressed how the combined effect of blood viscosity and turbulence models affects hemodynamic results, in this case by analyzing turbulent-transition at different Reynolds numbers on a backward facing step. This work, however, did not address if WSS was affected and considered an idealized geometry which greatly differs from a realistic aorta.

To bridge the gap between the studies which have assessed the influence of model choices independently, we present in this work an analysis focused on quantifying the combined effect of turbulence and viscosity models on wall-shear derived biomarkers for ATA using a patient-specific geometry and physiological boundary conditions. Up to date, no study has evaluated how viscosity models influence turbulence models and vice versa. Hence, this work presents a novel analysis of the combined effect of modeling assumptions on aortic flows and provides the optimal modeling strategy to obtain accurate WSS biomarkers. We will assess the effect of considering Newtonian or Carreau fluid models in combination with the absence or presence of a Dynamic Smagorinsky-Lilly (DSL) subgrid-scale turbulence model. The differences between CFD computations considering a healthy and a stenosed aortic valve will be evaluated in terms of time averaged wall shear stress (TAWSS), peak systole wall shear stress (PSWSS), oscillatory shear index (OSI) and shear angle (SA). TAWSS and PSWSS quantify the shear stress magnitude, OSI the fluctuations on the near-wall flow direction and SA the presence of rotating or reversed flow. This work presents the first analysis of the combined effect of turbulence and viscosity model on TAWSS, PSWSS, OSI and SA on ascending aorta simulations.

2. Method

2.1. Geometry

A gated-CT scan with a voxel size of [0.3125, 0.3125, 0.75] mm from a patient suffering from ascending thoracic aortic aneurysm was segmented using a semi-automatic procedure based on local thresholding as described in (37) and manually corrected using 3D Slicer. The procedure was performed complying with the ethical standards. A smoothing and remeshing procedure was performed in order to reduce the triangulation size to a size of 0.2 mm in order to remove any staircase artifacts while preserving the segmentation details, as shown in Figure 1.

The centerline of the aorta was then extracted using the Vascular Modelling Toolkit (38). A cylinder was positioned at the aortic root and aligned with the centerline, providing a planar surface over which an idealized 2-D tricuspid valve shape was projected , as shown in Figure 1c. The valve geometry was obtained from a previous work (39). Two aortic valves are herein investigated: a healthy and a stenosed valve with an orifice area of 300 mm^2 and 150 mm^2 respectively, obtained after scaling the idealized shape. Supra-aortic vessels were extended five equivalent hydraulic diameters to prevent the presence of a recirculation region at the outlets. The ascending aortic wall was identified as the region between the sinotubular junction and the brachiocephalic ostium. We divided the ascending section into external (greater curvature) and internal (lesser curvature) walls by projecting the centerline onto the surface, as depicted in Figure 1b.

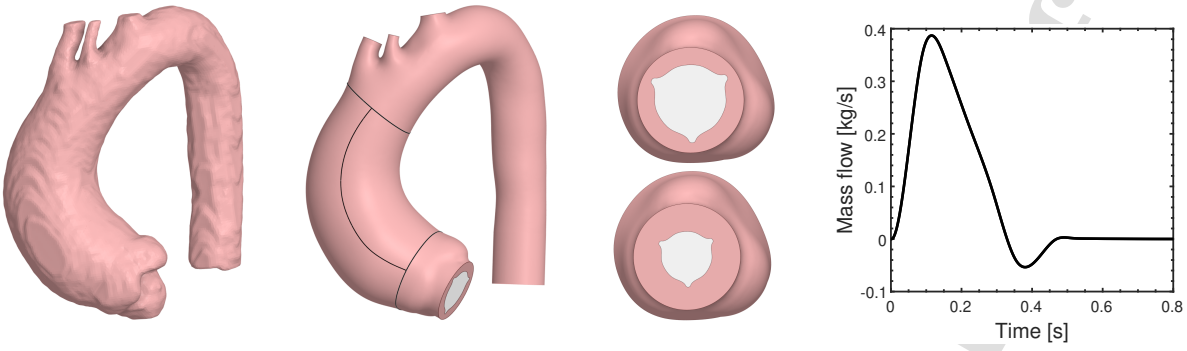

(a) (b) (c) (d)

Figure 1: Geometric details of the segmentation (a), processed geometry (b), projections of healthy and stenosed valves (c) and mass flow through the aortic valve (d).

2.2. Computational model and boundary conditions

A polyhedral mesh was used to discretize the resultant geometry, as it enables to obtain good cell-quality and smooth transitions in curved and irregular surfaces as those present in many aneurysms. Both meshing and computing stages were performed using Ansys Fluent 22.1 (ANSYS Inc., Canonsburg, PA, USA).

An idealized mass flow profile was used to impose the inlet condition, considering a cardiac cycle of duration $T = 0.8$ s, a peak flow of 0.387 kg/s and mean flow of 4.83 l/min, as depicted in Figure 1d. The spatial velocity-distribution profile imposed through the idealized valve corresponded to a fully developed turbulent flow obeying a $1/7^{\text{th}}$ power-law (40; 41), as it yields a compromise between plug and parabolic profiles. The systolic jet Reynolds was 1.0×10^4 and 7.2×10^3 for the stenosed and healthy valve respectively, corresponding to a jet-center velocity of 3 and 1.5 m/s. In the absence of MRI flow data one cannot justify which profile better represents the patient's flow, as the jet profile is unique to each individual and large variability can be observed across a population, especially in the cases with aortic stenosis (42; 43; 44).

A three-element RCR windkessel boundary condition was imposed at the outlets. The parameters were tuned to ensure a predefined pulse pressure, set to 40 mmHg, and a distribution of flow proportional to the outlet areas as described in (45). The equations for the windkessel components were solved using a second order backward differencing scheme which has been validated against analytical solutions (46).

2.3. Turbulence modelling

To capture and assess the effect of turbulence, we included the DSL subgrid-scale model (47) and compared the results with the case where the subgrid model was absent, which, for convenience, will be referred hereafter as laminar flow model (LFM).

On both cases, the Navier-Stokes (N-S) equations for an incompressible fluid are used to resolve the flow dynamics. When considering the LFM, no viscous losses below the grid-resolved flow are considered. However, when considering the DSL model, an additional term is added to the momentum equation in order to model the viscous energy loss associated with the subgrid scale eddies, leading to the filtered N-S for the grid-resolved velocity field ($\bar{u}$). The filtered continuity and momentum equations can thus be rewritten as:

$$\frac{\partial \bar{u}_i}{\partial x_i} = 0\,, \tag{1}$$

$$\frac{\partial \bar{u}_i}{\partial t} + \bar{u}_j \frac{\partial \bar{u}_i}{\partial x_j} = -\frac{1}{\rho}\frac{\partial \bar{p}}{\partial x_i} + \nu \frac{\partial}{\partial x_j}\left(\frac{\partial \bar{u}_i}{\partial x_j}\right) - \frac{\partial \tau_{ij}}{\partial x_j}\,, \tag{2}$$

where p is the pressure, ρ the density, ν the kinematic viscosity and τ_{ij} the subgrid scale turbulent stress tensor which models the dissipation due to subgrid scale eddies. The subgrid-scale model employs the Boussinesq hypothesis to compute the sub-grid stresses:

$$\tau_{ij} - \frac{1}{3}\tau_{kk}\delta_{ij} = -2\nu_{sgs}\bar{S}_{ij}\,, \tag{3}$$

where $\bar{S}_{ij} = \frac{1}{2}\left(\frac{\partial \bar{u}_i}{\partial x_j} + \frac{\partial \bar{u}_j}{\partial x_i}\right)$ is the grid-resolved strain rate and ν_{sgs} the subgrid eddy viscosity, which is computed considering the Smagorinsky constant C_S and the local grid scale Δ as:

$$\nu_{sgs} = (C_S\Delta)^2|\bar{S}|. \tag{4}$$

The choice for using the dynamic subgrid-scale model over the standard Smagorinsky-Lilly or the WALE model, the latter being specifically designed to accurately capture the asymptotic behaviour of wall bounded flows, is due to the pulsating nature of the cardiac flow. The large variability of the velocity field makes it difficult to define a static Smagorinski or WALE constant that would accurately model the turbulent viscosity across the spatio-temporal domain. The DSL model allows to update the Smagorinsky constant dynamically by accounting for the instantaneous velocity field to define a second filter for the equations of motion, providing a space and time varying C_S to better model the subgrid eddy viscosity. Moreover, the double-filtering process allows to compute the contribution of the small scale eddies and identify regions of laminar flow, where the subgrid viscosity will be effectively zero, enabling the model to reconstruct laminar to turbulent transition.

On the computations where DSL subgrid-scale model was active, we used SIMPLEC for the pressure-velocity coupling scheme. Second order and bounded central differencing were used to discretize pressure and momentum terms respectively, the later being chosen due to its low numerical diffusion. For the case where subgrid-scale model was absent, PISO was used for the pressure-velocity coupling and second order differencing for both momentum and pressure terms. In both cases, a second order implicit scheme was used for temporal discretization and a time step of 0.1 ms, ensuring a Courant-Friedrichs-Lewy number below unity. At the inlet, no synthetic turbulence was imposed to ensure equal boundary conditions in all scenarios.

2.4. Viscosity

The fluid viscosity was modeled considering both a constant viscosity $\mu_c = 3.5$ mPa·s and a shear-thinning Carreau model (48), commonly used in literature, defined as

$$\mu(\dot{\gamma}) = \mu_\infty + (\mu_0 - \mu_\infty)\left[1 + (\lambda\dot{\gamma})^2\right]^{\frac{n-1}{2}}, \tag{5}$$

where the time constant $\lambda = 3.313$ s, Power-Law index $n = 0.3568$, zero shear viscosity $\mu_0 = 56$ mPa·s and infinite shear viscosity $\mu_\infty = 3.5$ mPa·s. The non-NV allows to account for the increased viscosity in low velocity regions, which could in turn affect the wall shear stress (WSS) values and the evolution of the flow structure. Fluid density was set to 1056 kg/m^3.

2.5. WSS biomarkers

Numerous hemodynamic indices appear in literature, however, we have limited our study to four wall shear derived biomarkers, namely: timed average WSS (TAWSS), peak systole WSS (PSWSS), oscillating shear index (OSI) and shear angle (SA). TAWSS reveals the averaged magnitude of the wall shear and is described by the following equations:

$$\text{TAWSS} = \frac{1}{T}\int_0^T |\mathbf{WSS}(t)|\, dt, \tag{6}$$

where T represents the duration of one cardiac cycle. PSWSS is the magnitude of the WSS field at peak systole, which occurs at 0.12 s. The OSI describes the oscillations on shear direction. When low, the flow over a given node follows a predominant direction and, when high, the flow direction fluctuates during the cardiac cycle. It is defined according to:

$$\text{OSI} = 0.5\left(1 - \frac{\left|\int_0^T \mathbf{WSS}(t)\, dt\right|}{\int_0^T |\mathbf{WSS}(t)|\, dt}\right). \tag{7}$$

Mesh parameter	Coarse	Medium	Fine
Face size (mm)	0.50	0.35	0.25
Max. element size (mm)	1.00	0.70	0.50
No. of elements (10^6)	2.23	4.08	7.93

Table 1
Mesh parameters.

The SA defines the directionality of the wall shear vector and is used to reveal the the presence of rotating and backward flow. It will be evaluated at peak systole and is defined as:

$$\mathrm{SA} = \frac{2}{\pi}\arctan\left(\frac{\mathrm{WSS_{Axial}}}{\mathrm{WSS_{Circ}}}\right), \tag{8}$$

where axial and circumferential shear, $\mathrm{WSS_{Axial}}$ and $\mathrm{WSS_{Circ}}$ respectively, are defined by decomposing the WSS according to the centerline direction. $\mathrm{WSS_{Axial}}$ has a positive sign when the flow progresses along the aorta and a negative in the presence of reversed flow, while $\mathrm{WSS_{Circ}}$ takes only positive values as an analysis of clockwise and anticlockwise shear pattern is not considered in this study. For the analysis, nodal positions along the aorta were normalized such that 0 corresponds to the sinotubular junction, and 1 to the brachiocephalic ostium.

3. Results

In this section we first assess the mesh requirements for this study. Secondly, we perform a cycle-convergence analysis to reveal the minimum number of cycles required to guarantee that the results have sufficiently converged to a constant value. Finally, we present the results obtained considering both a healthy and stenotic valve in terms of TAWSS, systolic WSS, systolic SA and OSI.

3.1. Mesh convergence

As a first step, a mesh convergence study will be performed considering the stenosed valve and the DSL subgrid model, in order to establish the mesh requirements on the most restrictive case where higher turbulence and velocity is expected. For this analysis the Carreau viscosity (CV) model was chosen as it provides a more faithful description of blood behaviour. For all meshes, the inflation layer is composed of 15 hexagonal prisms and the first layer cell height adjusted to ensure an aspect-ratio of 7. The mesh parameters are summarized in Table 1. Orthogonal mesh quality was above 0.9 in 99.5% of the domain in all meshes.

The mesh convergence analysis was performed by evaluating the TAWSS on both the internal and external walls. The TAWSS difference was obtained by subtracting the results from the fine mesh from the results of the coarse and medium meshes, as depicted in Figure 2. It was necessary to interpolate the results from the coarse and medium meshes onto the fine mesh in order to enable a node-to-node comparison. We can observe that the medium mesh is capable of

resolving the flow structure near the wall with sufficient detail, with a mean error of 0.11 Pa and a maximum node-to-node difference of [-0.89, 0.59] Pa. In the case of the coarse mesh, the mean error was 0.25 Pa and maximum difference [-1.81, 1.01] Pa. The circumferentially averaged values along the centerline for both the internal and external walls are shown in Figure 2. We can observe how the difference between fine and medium meshes is negligible, whereas the coarse mesh underestimates significantly the averaged values in the external wall. In view of these results, we consider the medium mesh capable of resolving the flow with sufficient detail for the present study.

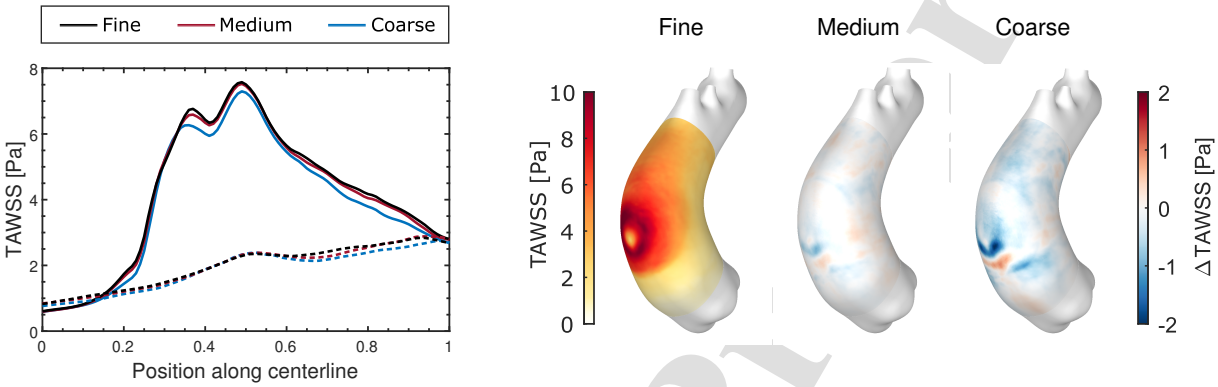

Figure 2: Averaged values of TAWSS along centerline for the external (solid) and internal (dashed) walls (left), contours of TAWSS on the fine mesh and contours of TAWSS difference with respect to fine mesh for medium and coarse mesh (right).

3.2. Cycle convergence

The cardiac cycle accounts for a systole and a diastole and, in the aorta, this is reflected as a fast accelerating and decelerating phase. Under these conditions, the flow develops a chaotic structure and significant variations can be observed between cycles. The flow structure present at the end of the previous cardiac cycle initializes the flow field for the following cycle and can significantly influence the new eddy structure.

Since this work is focused on performing an accurate and isolated analysis on the turbulence and viscosity models, we must ensure that the cycle averaged results are sufficiently converged. The cycle-to-cycle variation of the time averaged field variables must be sufficiently small to negligibly affect the model comparison. In this way we ensure a fair analysis in which no uncontrolled phenomena may mask the results.

We assessed the cycle requirements considering the LES-CV model. We performed 41 cardiac cycles and computed the TAWSS_i for the cycles $i \in [2, 40]$ considering the interval $[T,\ iT]$. The first cycle was excluded from the analysis. The error due to the considered cycles is computed as:

$$\delta_i = \frac{1}{N}\sum_{n=1}^{N} |\mathrm{TAWSS}_{i,n} - \mathrm{TAWSS}_{41,n}|, \tag{9}$$

being N the number of nodes on the wall. The evolution of δ_i and spatially-averaged TAWSS are depicted in Figure 3, together with the standard deviation (σ) of TAWSS after performing 41 cycles. Mean deviations in the TAWSS field fall below 0.05 Pa after performing 15 cycles. However, spatially-averaged values stabilize faster and lie within 3.29 ± 0.01 Pa of after completing 4 cycles. The highest variability across cycles is observed in the vicinity of the jet impingement region, having a maximum $\sigma = 0.71$ Pa. Significant variability, $\sigma = [0.3 - 0.6]$ Pa, can be observed in the central and superior sections of the ascending aorta. The deviation field $\Delta\text{TAWSS}_i = \text{TAWSS}_i - \text{TAWSS}_{41}$ is depicted in Figure 4. For the present study, after considering both δ and field variations, 20 cycles will be computed to guarantee that the WSS field has stabilized.

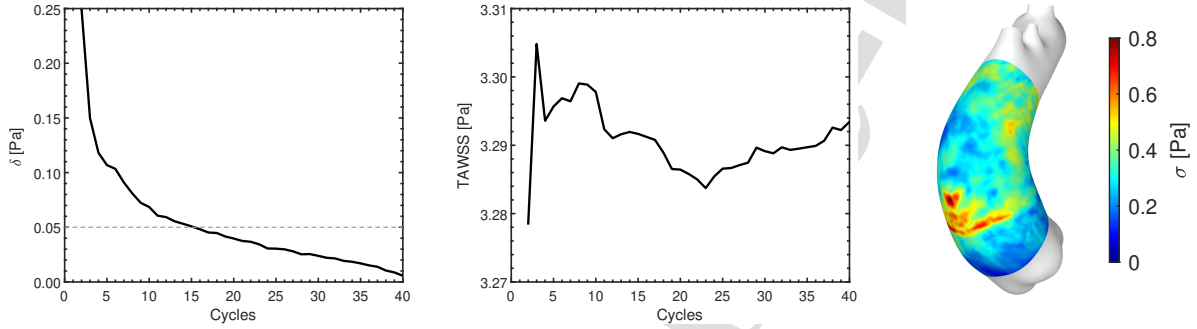

Figure 3: Cycle convergence analysis: δ_i (left) and spatially-averaged TAWSS (center) according to number of cycles and contours of the standard deviation of TAWSS after 41 cycles (right).

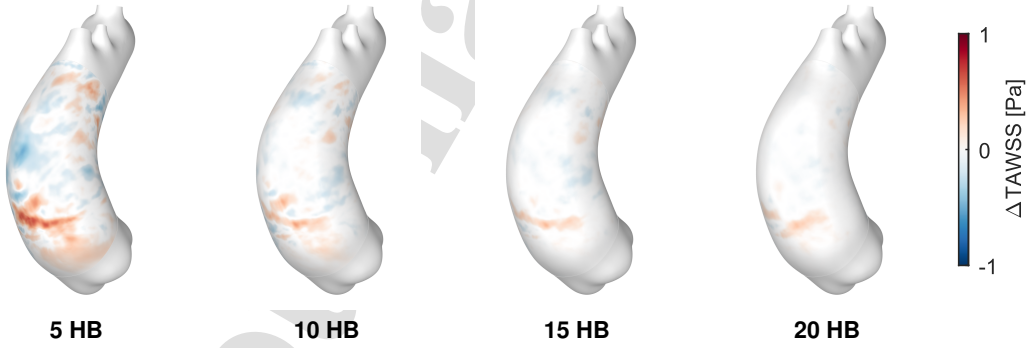

Figure 4: Cycle convergence analysis: Contours of local TAWSS error.

3.3. Viscosity and turbulence analysis

In order to fully understand the effect of the different viscosity and turbulent models on aorta simulations, we need to analyze the different flow regimes that can be commonly observed in patients. One of the most important factors

Variable	Valve	LES-CV	LES-NV	LFM-CV	LFM-NV
TAWSS	Healthy	1.80	1.71	1.81	1.73
	Stenotic	3.29	3.13	3.27	3.18
PSWSS	Healthy	2.06	1.93	2.08	1.94
	Stenotic	5.09	4.84	5.14	4.96
OSI	Healthy	0.267	0.267	0.270	0.270
	Stenotic	0.247	0.245	0.245	0.252

Table 2
Spatially averaged values for the modeled scenarios.

Variable	Valve	LES-NV	LFM-CV	LFM-NV
TAWSS	Healthy	-5.04	0.10	-4.37
	Stenotic	-4.65	-0.48	-3.36
PSWSS	Healthy	-6.14	1.19	-5.50
	Stenotic	-5.01	0.94	-2.63
OSI	Healthy	0.19	1.35	1.30
	Stenotic	-0.79	-0.91	2.05

Table 3
Relative difference of spatially averaged values for the modeled scenarios with respect to the LES-CV case.

which influences the flow regime is the stenosis severity, where fusion and stiffening of aortic valve leaflets causes the orifice to deform and reduce. Due to this, two scenarios are explored: a healthy and a stenotic valve.

In favour of clarity and to facilitate the analysis of the differences, the contours for each biomarkers β will be depicted only for LES-CV, whereas for the remaining cases only the difference with respect to the LES-CV will be depicted as $\Delta\beta_{case} = \beta_{\text{case}} - \beta_{\text{LES-CV}}$. A summary of the mean value and relative difference of the field variables is summarized in Tables 2 and 3.

3.3.1. Time averaged WSS

The distribution of TAWSS exhibits a similar pattern for both valves, consisting of a circular region with elevated TAWSS on the central part of the external wall, which coincides with the jet impingement region where fast moving flow expands from the collision zone upwards and sideways, creating a region with intermediate shear, as depicted in Figure 5. Notable differences can be observed between the two valves, as values in the high shear region range between 2 to 4 and 6 to 10 Pa in the healthy and stenotic case respectively. The high shear region is more compact and defined in the stenotic case. For both valve conditions, the differences between the reference LES and the laminar models reveal that the LES achieves a greater dispersion of the high shear region, as on the LFM contours we can observe a negative (blue) band surrounding the inferior border of this high shear region. Considering all the models, the mean TAWSS value for the healthy and stenotic valve was, respectively, 1.762 and 3.22 Pa, with a standard deviation of 0.050 and 0.075 Pa. We observe a larger deviation in the stenotic scenario.

Assessing the viscosity effect reveals that both CV cases develop higher TAWSS with respect to their NV counterparts. Under stenotic conditions, assuming NV causes an underestimation of 4.7% (LES) and 2.9% (LFA).

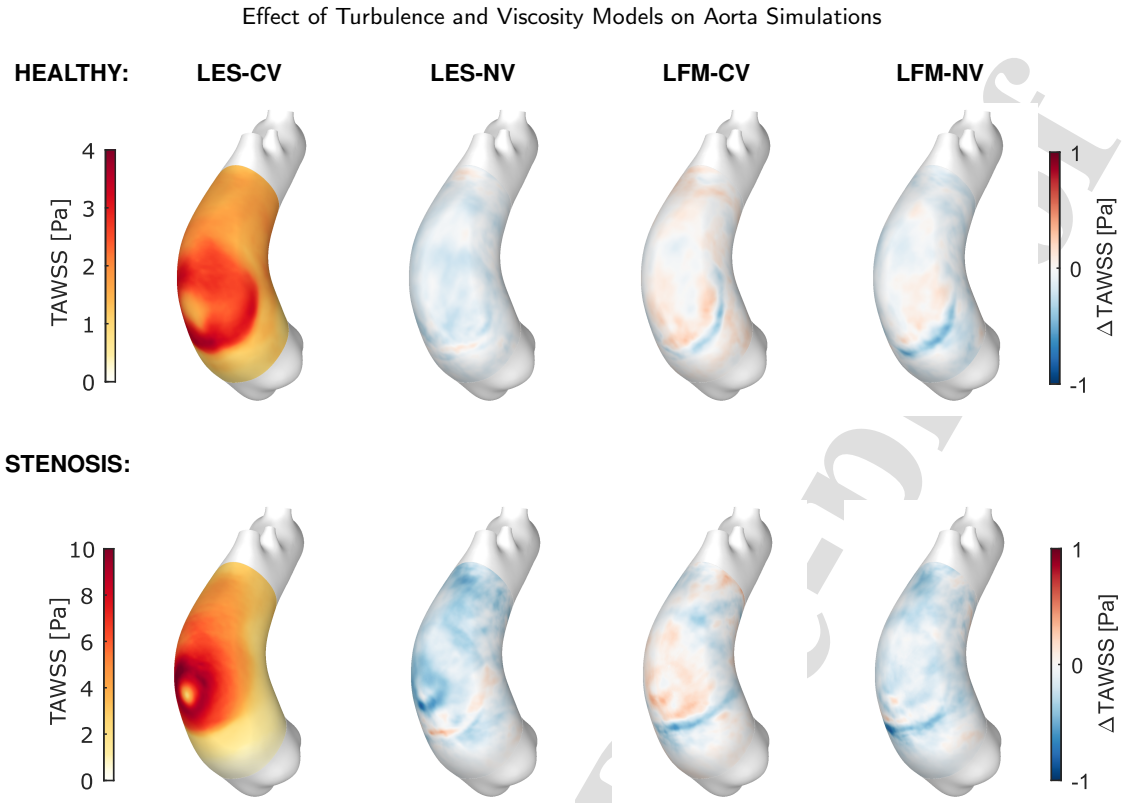

Figure 5: TAWSS for healthy (top) and stenotic valve (bottom).

This holds for the healthy condition: underestimation of 5.0% (LES) and 4.5% (LFA). Turbulence model assessment reveals that, under CV, the LFM exhibits differences below 0.5% from its LES counterpart, whereas under NV, the LFM overestimates TAWSS by 0.7-1.4%. This indicates that accounting for non-NV has a greater impact than accounting for a subgrid model. Furthermore, it is revealing to observe the impact of the viscosity model is amplified under a LES turbulence model, since the difference between LES models (4.7-5.0%) is greater than between LFM models (2.9-4.5%). In order to gain further insight into these differences, the circumferentially averaged values along the centerline are plotted for both internal and external walls on Figure 6. The best match of LES-CV is obtained when considering a LFM-CV model, which is in agreement with the values given in Table 3.

To better understand viscous phenomena, we define the non-Newtonian importance factor (49) as the ratio between the dynamic viscosity and the Newtonian viscosity: $IF = \mu/\mu_\infty$. The systolic and time averaged IF are given in Table 4. The values of IF are higher for LES models under both valve conditions, which shows that the importance of non-NV depends on the turbulence model used. Accounting for subgrid viscosity alters the eddy development and thus the shear rate in the vicinity of the wall, which in turn determines the fluid viscosity and the IF.

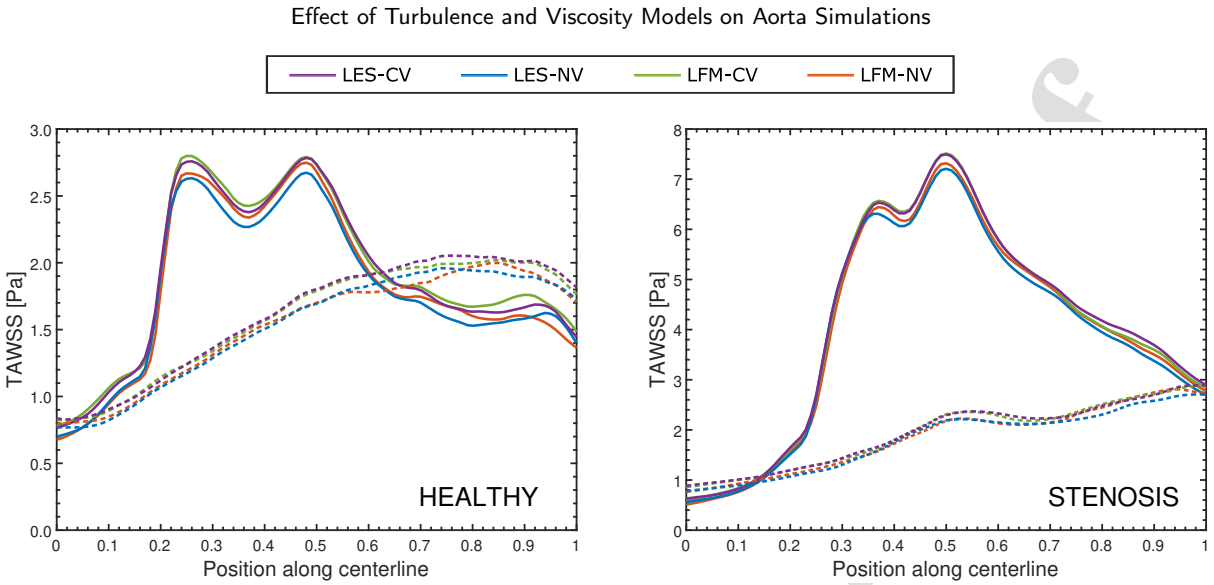

Figure 6: Averaged values of TAWSS along centerline for the external (solid) and internal (dashed) walls for the case with healthy (left) and stenotic (right) valve.

Turbulence model	Healthy		Stenosis	
	Systole	TA	Systole	TA
Laminar	1.160	1.277	1.148	1.290
LES	1.165	1.286	1.166	1.297

Table 4
Non-Newtonian importance factor under LES and laminar turbulence models for healthy and stenotic valves.

3.3.2. Peak systole WSS

The systolic WSS depicted in Figure 7 reveals distinct patterns between the valve types. In the healthy case, low values are observed along the aortic wall with the exception of the sinotubular junction. This contrasts with the stenosed case, where we can clearly observe the characteristic features that result from the jet impinging on the wall. This can be explained since a healthy valve results in a lower jet velocity and therefore the time required for the jet to develop and arrive to the wall is higher. For the stenotic case, a highly-localized high shear region on the external wall can be observed, with the remaining aorta subject to low shear levels.

A predominant underestimation of shear on both NV cases can be observed, similarly to the observation on TAWSS. The LFM-CV shows smaller differences as confirmed by Table 3, with the PSWSS being overestimated by 1.2% and 0.9% for the healthy and stenotic valve conditions respectively. The IF at peak systole, given in Table 4, is higher on LES models, as occurred for TAWSS.

3.3.3. Shear angle

The SA reveals different patterns for each valve type. Considering the healthy valve, the direction of the systolic WSS reveals a region with reversed flow in the central section of the aorta, as indicated by the negative SA values on

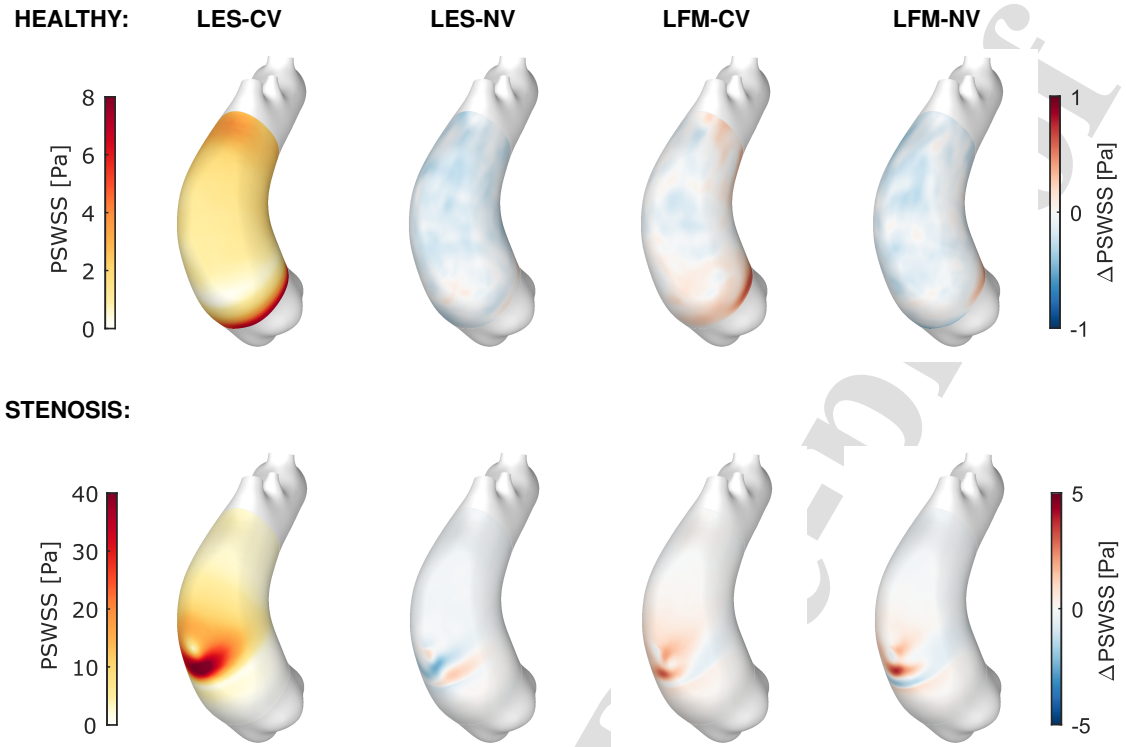

Figure 7: PSWSS for healthy (top) and stenotic valve (bottom).

Figure 8. As can be observed, in all models the shear direction is identical throughout the domain with the exception of a banded region where the reversed flow of the midsection collides with the advancing flow emerging from the sinotubular junction. The banded stripes depicted in the ΔSA plots indicate that the collision band is minimally distorted. Considering the Lam-New case, which exhibits the largest differences, the maximum width of the band is 2.6 mm. When analyzing the stenotic valve, reversed flow can be observed in the inferior section of the external wall. The rest of the aorta wall has a positive SA close to 1, with the exception of the region where the jet impinges the wall, where the SA ranges between [0, -0.5]. On the LES-NV case the reversed flow region is slightly retreated, approximately 1 mm, whereas on the laminar cases the reversed flow regions has advanced 1-2 mm. The results of SA suggest that, although the levels of WSS might be altered by the modelling assumption, the WSS direction at peak systole is preserved.

3.3.4. Oscillating shear index

The OSI of the reference LES-CV case reveals similar patterns on both valve scenarios, as depicted in Figure 9. The central section of the external wall is exposed to low OSI levels inferior to 0.1, which coincides with the high TAWSS region. This low OSI region is surrounded by high OSI which coincides with the low TAWSS. This can be related to the directional dominance of the impinging jet which produces a well defined flow pattern over the wall directed upstream.

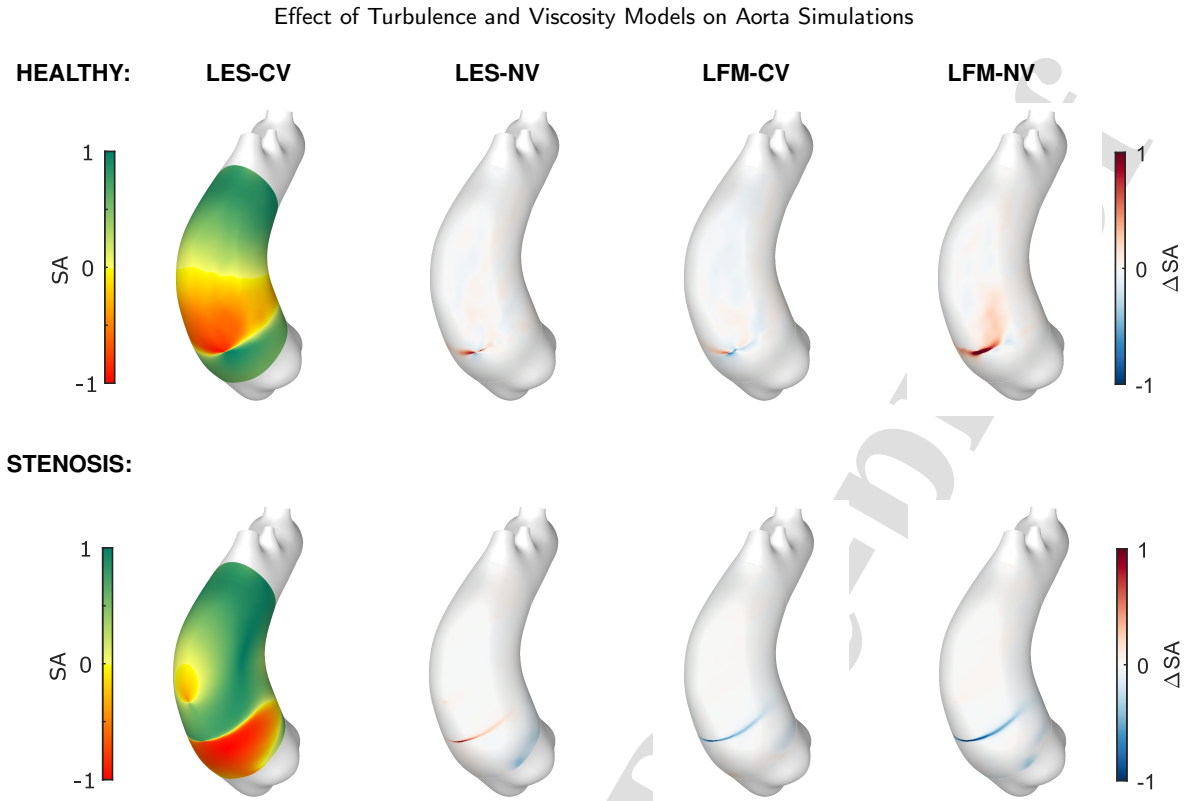

Figure 8: SA for healthy (top) and stenotic valve (bottom).

On the contrary, the inferior section is subject to reversed flow and the creation of a recirculating region, where the flow pattern is disrupted. The region surrounding the jet impingement is exposed to decaying vortexes which travel along the wall with reduced energy and higher instabilities, leading to a more chaotic flow structure. The combination of low TAWSS and continuous flow disruption inevitably leads to the creation of a high OSI region.

The comparison between models shows a good agreement on the low OSI central region of the external aortic wall for both valve scenarios. Despite the local differences on the lower section of the aortic wall, all cases exhibit high OSI levels on the inferior section. On the region surrounding the ostium, variations can also be observed. The deviations on Figure 9 reveal a complex pattern which impedes further conclusions. The values in Table 3 reveal smallest averaged discrepancies when considering the LES-NV (<0.8%) and biggest when considering LFM (0.9-2.1%).

4. Discussion

In this work, we have quantified the combined effect of LES and non-NV on WSS derived biomarkers and concluded that including non-NV has a greater impact on the results in comparison to the inclusion of the LES subgrid model. We observed a reduction on the TAWSS and PSWSS when considering NV which agrees with previous studies (21; 50; 51). Spatially averaged values showed that TAWSS is underestimated by 4.7-5.0% if constant viscosity is assumed under

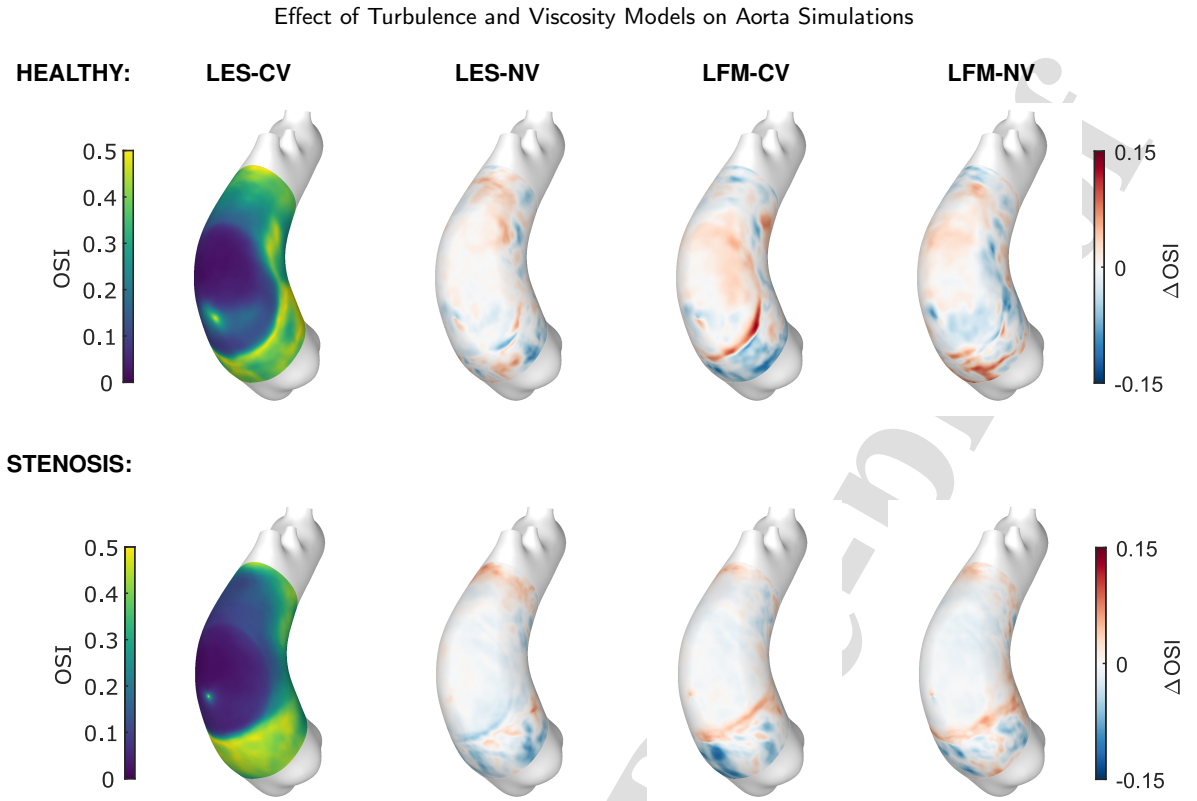

Figure 9: OSI for healthy (top) and stenotic valve (bottom).

a LES model, although this value drops to 2.9-4.5% when considering a laminar model. The reduction in WSS due to NV could be explained by a nonphysical reduced viscosity in the vicinity of the wall. As we approach the wall the velocity asymptotically decreases to zero thus the non-Newtonian behaviour is magnified. Non-Newtonian effects become more apparent in low velocity regions and it is thus vital to account for this shear dependent viscosity when accurately modeling biochemical processes. For example, it has been proven that non-NV should be modeled when analysing lipoprotein deposition in regions with flow recirculation (51), platelet activation potential (21) and monocyte adhesion to endothelial cells on atherosclerotic lesion (50). The IF has revealed a slight increase of non-Newtonian effects when considering the LES model under both valve conditions, which could account for the larger differences in WSS between the LES cases. It is possible that the subgrid viscosity, which contributes to dissipating the eddy structure, leads to a diminished velocity field which amplifies the non-Newtonian phenomena in the LES scenarios.

Differences between turbulence models with an equal viscosity model are surpassed by the differences between viscosity models with an equal turbulence model, as shown in Table 3. Two interesting findings regarding the combination of viscosity and turbulence models are worth mentioning. Firstly, the impact of the turbulence model is greater when considering a NV and, secondly, the impact of non-NV is greater when including a subgrid turbulence model. Despite this, we have observed that the turbulence model has a marginal impact on the results and we conclude

that high resolution laminar models are capable of sufficiently resolving the flow dynamics, as the relative difference in TAWSS for LFM-CV is below 0.5%, agreeing with the results of (31). Although spatially-averaged values show limited discrepancies due to turbulence model choice, we must consider that the additional subgrid viscosity provided by the LES model affects the eddy development and breakdown which consequently alters the WSS pattern along the wall, as shown in Figure 5. A final consideration in this regard is that both the laminar and LES computations required equivalent computational resources, hence no clear benefit is gained by considering a laminar model.

At present, no study has examined the discrepancies on SA. Our results have shown that SA exhibits negligible differences amongst the considered models, one possible explanation being that the SA is defined by the bulk flow pattern, which is mainly determined by the jet profile and only marginally by the modelling assumptions.

The results of OSI exhibit significant deviations amongst the studied models. The differences due to the viscosity assumptions agree with (52), however this study focused on abdominal aneurysm where the Re is lower and the flow profile has damped temporal variability. Despite the OSI discrepancies between the herein considered models, the pattern consisting of a low OSI region in the external wall surrounded by high OSI is preserved in all cases. Since OSI quantifies the flow direction fluctuations and regions exposed to vortexes are exposed to chaotic flow disruptions, it is possible that the analysis on high OSI regions would benefit from computing additional cycles in order to obtain a smoother comparison.

The present study exposes the importance of assessing different aortic valve conditions as the flow structure and WSS patterns are severely affected by the jet characteristics. Thus, studies focused on computational strategies should be performed on a wide range of flow conditions.

We have observed that significant differences can appear on the herein analyzed set of fluid biomarkers. However, it is surprising that these differences can be just as important as the cycle-to-cycle variations that occur if insufficient cycles are considered for the time averaging process. This is due to the differences in the flow structure present in the fluid domain before each cardiac cycle begins. The flow of the previous cycle conditions how the flow will develop during the following cycle. Thus, when comparing different models and computational strategies, we must ensure that the time averaged results have sufficiently stabilized in order to not mask the differences caused by the numerical methods alone. This work suggests that studies focused on evaluating the effect of numerical methodologies should be performed considering a minimum of 15 cardiac cycles to ensure errors in TAWSS remain below 0.05 Pa. As much as the difference between models may seem considerable, it is obvious that the differences between the healthy and stenosis valves are much more significant. Since the biomarker distribution pattern is preserved in all cases, the choice of model has minimal impact in comparison to including a spatially and temporally calibrated jet (53). However this may be, our results demonstrate the importance of considering appropriate turbulence and viscosity models when developing in-silico hemodynamic analyses for the ATA. The effect of the model combinations has been quantified and

could serve to justify modelling assumptions when dealing with ATA simulations and potentially aid in establishing standardized workflows for clinical applications.

4.1. Limitations

We did not tackle on this analysis the differences in turbulent kinetic energy in the flow as we decided to exclusively analyse the wall shear derived biomarkers. Previous studies have analyzed turbulence and its dependency on the modelling assumptions including valve shape and jet velocity (40) and different turbulence models (32; 34).

It is fair to criticize the choice of an idealized valve shape for the healthy and, specially, the stenosed case since idealized shapes such as the one herein presented are rarely observed in real patients. However, our work was not intended to precisely characterize a patient specific condition but rather to compare the influence of the modelling assumptions in a rigorous manner. Moreover, we have performed this analysis using a projection of the valve opening and imposing a spatially varying profile, rather than modelling the 3D structure of the valve leaflets. This simplification has a direct effect on the flow structure, specially in terms of turbulence generation (40). Further analysis is required to correctly understand the effect of modelling choices under patient-specific conditions, such as highly stenosed patients with highly irregular valve opening. Furthermore, the effect of the modelling assumptions would differ if we accounted for wall and valve motion, as it has been proven that the FSI effect significantly alters WSS (54).

It is clear that numerous improvements can be incorporated in a pursuit of fidelity. However, we must consider that not all biomarkers require an equal modelling complexity to provide the necessary insight to aid clinicians during the diagnosis. By understanding the influence which modelling assumptions have on the results, one is capable of establishing a justified balance between accuracy requirements and modelling complexity. Achieving this balance is of vital importance as higher complexity implies increased computational cost, an issue which is currently limiting the expansion of computational tools for clinical use.

5. Conclusions

In this work, a thorough analysis of the combined effect of viscosity and turbulence models on WSS biomarkers has been performed. Firstly, it has revealed that non-NV have a greater impact on WSS than LES subgrid model. In addition, NV has shown to cause an underestimation of shear levels: 4.7-5.0% considering LES, 2.9-4.5% considering LFM. We thus encourage the use of non-NV for ATA simulations as it will prevent underestimation of WSS. It is noteworthy that the contribution of a non-NV is amplified when combined with a subgrid model, as can be concluded from the larger differences in TAWSS exhibited between LES models than between laminar models. This finding indicates that the LES model is augmenting the non-Newtonian behaviour of the fluid. Overall, in all scenarios the biomarkers followed a similar distribution along the aortic wall, where the main differences were due to a distinct

expansion and decay of the jet along the wall. Lastly, it is revealing to observe that the cycle-to-cycle variability has a significant impact if insufficient cycles are assessed and consequently can mask the differences between the numerical models. Be that as it may, a precise knowledge of the impact of the chosen modelling assumptions is mandatory if we pursue the development of a new generation of tools certified for clinical use, where the requirements of trustworthiness and reproducibility of results are of paramount importance.

6. Funding

The work has received funding from the European Union's Horizon 2020 research and innovation programme under the Marie Sklodowska-Curie grant agreement No 859836, MeDiTATe: "The Medical Digital Twin for Aneurysm Prevention and Treatment".

References

[1] Olufsen MS. Structured Tree Outflow Condition for Blood Flow in Larger Systemic Arteries. American Journal of Physiology-Heart and Circulatory Physiology. 1999;276(1):H257-68. PMID: 9887040. Available from: https://doi.org/10.1152/ajpheart.1999.276.1.H257.

[2] Pirola S, Cheng Z, Jarral OA, O'Regan DP, Pepper JR, Athanasiou T, et al. On the Choice of Outlet Boundary Conditions for Patient-Specific Analysis of Aortic Flow Using Computational Fluid Dynamics. Journal of Biomechanics. 2017 Jul;60:15-21. Available from: https://linkinghub.elsevier.com/retrieve/pii/S0021929017303007.

[3] Xiao N, Humphrey JD, Figueroa CA. Multi-Scale Computational Model of Three-Dimensional Hemodynamics within a Deformable Full-Body Arterial Network. Journal of Computational Physics. 2013 Jul;244:22-40. Available from: https://linkinghub.elsevier.com/retrieve/pii/S0021999112005475.

[4] Pappalardo F, Wilkinson J, Busquet F, Bril A, Palmer M, Walker B, et al. Toward A Regulatory Pathway for the Use of in Silico Trials in the CE Marking of Medical Devices. IEEE Journal of Biomedical and Health Informatics. 2022 Nov;26(11):5282-6. Available from: https://ieeexplore.ieee.org/document/9855387.

[5] ASME. ASME Standard, V&V 40–2018, Assessing Credibility of Computational Modeling through Verification and Validation: Application to Medical Devices; 2018. Available from: https://www.asme.org/codes-standards/find-codes-standards/v-v-40-assessing-credibility-computational-modeling-verification-validation-application-medical-devices.

[6] Capellini K, Vignali E, Costa E, Gasparotti E, Biancolini ME, Landini L, et al. Computational Fluid Dynamic Study for aTAA Hemodynamics: An Integrated Image-Based and Radial Basis Functions Mesh Morphing Approach. Journal of Biomechanical Engineering. 2018 08;140(11). 111007. Available from: https://doi.org/10.1115/1.4040940.

[7] Manchester EL, Pirola S, Salmasi MY, O'Regan DP, Athanasiou T, Xu XY. Analysis of Turbulence Effects in a Patient-Specific Aorta with Aortic Valve Stenosis. Cardiovascular Engineering and Technology. 2021 Aug;12(4):438-53. Available from: https://doi.org/10.1007/s13239-021-00536-9.

[8] Mendez V, Di Giuseppe M, Pasta S. Comparison of Hemodynamic and Atructural Indices of Ascending Thoracic Aortic Aneurysm as Predicted by 2-way FSI, CFD Rigid Wall Simulation and Patient-Specific Displacement-Based FEA. Computers in Biology and Medicine. 2018;100:221-9. Available from: https://www.sciencedirect.com/science/article/pii/S001048251830204X.

[9] Vignali E, Gasparotti E, Celi S, Avril S. Fully-Coupled FSI Computational Analyses in the Ascending Thoracic Aorta Using Patient-Specific Conditions and Anisotropic Material Properties. Frontiers in Physiology. 2021;12. Available from: https://www.frontiersin.org/articles/10.3389/fphys.2021.732561.

[10] Tomasi J, Le Bars F, Shao C, Lucas A, Lederlin M, Haigron P, et al. Patient-Specific and Real-Time Model of Numerical Simulation of the Hemodynamics of Type B Aortic Dissections. Medical Hypotheses. 2020;135:109477. Available from: https://www.sciencedirect.com/science/article/pii/S0306987719309764.

[11] Bonfanti M, Balabani S, Greenwood JP, Puppala S, Homer-Vanniasinkam S, Díaz-Zuccarini V. Computational Tools for Clinical Support: a Multi-Scale Compliant Model for Haemodynamic Simulations in an Aortic Dissection Based on Multi-Modal Imaging Data. Journal of The Royal Society Interface. 2017;14(136):20170632. Available from: https://royalsocietypublishing.org/doi/abs/10.1098/rsif.2017.0632.

[12] Xu H, Piccinelli M, Leshnower BG, Lefieux A, Taylor WR, Veneziani A. Coupled Morphological–Hemodynamic Computational Analysis of Type B Aortic Dissection: A Longitudinal Study. Annals of Biomedical Engineering. 2018 Jul;46(7):927-39. Available from: http://link.springer.com/10.1007/s10439-018-2012-z.

[13] Andersson M, Karlsson M. Characterization of Anisotropic Turbulence Behavior in Pulsatile Blood Flow. Biomechanics and Modeling in Mechanobiology. 2021 Apr;20(2):491-506. Available from: https://link.springer.com/10.1007/s10237-020-01396-3.

[14] Andersson M, Ebbers T, Karlsson M. Characterization and Estimation of Turbulence-Related wall Shear Stress in Patient-Specific Pulsatile Blood Flow. Journal of Biomechanics. 2019;85:108-17. Available from: https://www.sciencedirect.com/science/article/pii/S0021929019300508.

[15] Xu L, Yin L, Liu Y, Liang F. A Computational Study on the Influence of Aortic Valve Disease on Hemodynamics in Dilated Aorta. Mathematical Biosciences and Engineering. 2020;17(1):606-26. Available from: https://www.aimspress.com/article/doi/10.3934/mbe.2020031.

[16] Jamaleddin Mousavi S, Jayendiran R, Farzaneh S, Campisi S, Viallon M, Croisille P, et al. Coupling Hemodynamics with Mechanobiology in Patient-Specific Computational Models of Ascending Thoracic Aortic Aneurysms. Computer Methods and Programs in Biomedicine. 2021 Jun;205:106107. Available from: https://linkinghub.elsevier.com/retrieve/pii/S0169260721001826.

[17] Capellini K, Gasparotti E, Cella U, Costa E, Fanni BM, Groth C, et al. A Novel Formulation for the Study of the Ascending Aortic Fluid Dynamics with in Vivo Data. Medical Engineering & Physics. 2020 Sep:S1350453320301387. Available from: https://linkinghub.elsevier.com/retrieve/pii/S1350453320301387.

[18] Lantz J, Gårdhagen R, Karlsson M. Quantifying Turbulent Wall Shear Stress in a Subject Specific Human Aorta using Large Eddy Simulation. Medical Engineering & Physics. 2012;34(8):1139-48. Available from: https://www.sciencedirect.com/science/article/pii/S135045331100316X.

[19] Beris AN, Horner JS, Jariwala S, Armstrong MJ, Wagner NJ. Recent Advances in Blood Rheology: a Review. Soft Matter. 2021;17:10591-613. Available from: http://dx.doi.org/10.1039/D1SM01212F.

[20] Hall JE. Guyton and Hall Textbook of Medical Physiology. Twelfth ed. Saunders; 2010.

[21] Lynch S, Nama N, Figueroa CA. Effects of Non-Newtonian Viscosity on Arterial and Venous Flow and Transport. Scientific Reports. 2022 Nov;12(1):20568. Available from: https://www.nature.com/articles/s41598-022-19867-1.

[22] De Vita F, de Tullio MD, Verzicco R. Numerical Simulation of the Non-Newtonian Blood Flow Through a Mechanical Aortic Valve. Theoretical and Computational Fluid Dynamics. 2016 Apr;30(1):129-38. Available from: https://doi.org/10.1007/s00162-015-0369-2.

[23] van Wyk S, Prahl Wittberg L, Bulusu KV, Fuchs L, Plesniak MW. Non-Newtonian Perspectives on Pulsatile Blood-Analog Flows in a 180° Curved Artery Model. Physics of Fluids. 2015 Jul;27(7):071901. Available from: http://aip.scitation.org/doi/10.1063/1.4923311.

[24] Biswas D, Casey DM, Crowder DC, Steinman DA, Yun YH, Loth F. Characterization of Transition to Turbulence for Blood in a Straight Pipe Under Steady Flow Conditions. Journal of Biomechanical Engineering. 2016 06;138(7). 071001. Available from: https://doi.org/10.1115/1.4033474.

[25] Khan MO, Valen-Sendstad K, Steinman DA. Direct Numerical Simulation of Laminar-Turbulent Transition in a Non-Axisymmetric Stenosis Model for Newtonian vs. Shear-Thinning Non-Newtonian Rheologies. Flow, Turbulence and Combustion. 2019 Jan;102(1):43-72. Available from: http://link.springer.com/10.1007/s10494-018-9905-7.

[26] Bahrani SA, Nouar C. Intermittency in the Transition to Turbulence for a Shear-Thinning Fluid in Hagen-Poiseuille Flow. Journal of Applied Fluid Mechanics. 2014;7(1):1-6. Available from: https://www.jafmonline.net/article_1416.html.

[27] Nadeem S, Akhtar S, Saleem A, Akkurt N, Ali Ghazwani H, Eldin SM. Numerical computations of blood flow through stenosed arteries via CFD tool OpenFOAM. Alexandria Engineering Journal. 2023;69:613-37. Available from: https://www.sciencedirect.com/science/article/pii/S1110016823001035.

[28] Akhtar S, Hussain Z, Nadeem S, Najjar IMR, Sadoun AM. CFD analysis on blood flow inside a symmetric stenosed artery: Physiology of a coronary artery disease. Science Progress. 2023;106(2):00368504231180092. PMID: 37292014. Available from: https://doi.org/10.1177/00368504231180092.

[29] Binter C, Gotschy A, Sündermann SH, Frank M, Tanner FC, Lüscher TF, et al. Turbulent Kinetic Energy Assessed by Multipoint 4-Dimensional Flow Magnetic Resonance Imaging Provides Additional Information Relative to Echocardiography for the Determination of Aortic Stenosis Severity. Circulation: Cardiovascular Imaging. 2017 Jun;10(6):e005486. Available from: https://www.ahajournals.org/doi/10.1161/CIRCIMAGING.116.005486.

[30] Dyverfeldt P, Hope MD, Tseng EE, Saloner D. Magnetic Resonance Measurement of Turbulent Kinetic Energy for the Estimation of Irreversible Pressure Loss in Aortic Stenosis. JACC: Cardiovascular Imaging. 2013 Jan;6(1):64-71. Available from: https://linkinghub.elsevier.com/retrieve/pii/S1936878X12008777.

[31] Manchester EL, Pirola S, Salmasi MY, O'Regan DP, Athanasiou T, Xu XY. Evaluation of Computational Methodologies for Accurate Prediction of Wall Shear Stress and Turbulence Parameters in a Patient-Specific Aorta. Frontiers in Bioengineering and Biotechnology. 2022 Mar;10:836611. Available from: https://www.frontiersin.org/articles/10.3389/fbioe.2022.836611/full.

[32] Xu L, Yang T, Yin L, Kong Y, Vassilevski Y, Liang F. Numerical Simulation of Blood Flow in Aorta with Dilation: A Comparisonbetween Laminar and LES Modeling Methods. Computer Modeling in Engineering & Sciences. 2020;124(2):509-26. Available from: https://www.techscience.com/CMES/v124n2/39535.

[33] Bozzi S, Dominissini D, Redaelli A, Passoni G. The Effect of Turbulence Modelling on the Assessment of Platelet Activation. Journal of Biomechanics. 2021 Nov;128:110704. Available from: https://linkinghub.elsevier.com/retrieve/pii/S0021929021004723.

[34] Parker LP, Svensson Marcial A, Brismar TB, Broman LM, Prahl Wittberg L. Computational Fluid Dynamics of the Right Atrium: A Comparison of Modeling Approaches in a Range of Flow Conditions. Journal of Engineering and Science in Medical Diagnostics and Therapy. 2022 Aug;5(3):031108. Available from: https://asmedigitalcollection.asme.org/medicaldiagnostics/article/5/3/031108/1140930/Computational-Fluid-Dynamics-of-the-Right-Atrium-A.

[35] Karimi S, Dabagh M, Vasava P, Dadvar M, Dabir B, Jalali P. Effect of Rheological Models on the Hemodynamics within Human Aorta: CFD Study on CT Image-Based Geometry. Journal of Non-Newtonian Fluid Mechanics. 2014;207:42-52. Available from: https:

//www.sciencedirect.com/science/article/pii/S0377025714000470.

[36] Kelly NS, Gill HS, Cookson AN, Fraser KH. Influence of Shear-Thinning Blood Rheology on the Laminar-Turbulent Transition over a Backward Facing Step. Fluids. 2020 Apr;5(2):57. Available from: https://www.mdpi.com/2311-5521/5/2/57.

[37] Geronzi L, Haigron P, Martinez A, Yan K, Rochette M, Bel-Brunon A, et al. Assessment of Shape-Based Features Ability to Predict the Ascending Aortic Aneurysm Growth. Frontiers in Physiology. 2023;14:378. Available from: https://www.frontiersin.org/articles/10.3389/fphys.2023.1125931.

[38] Antiga L, Steinman D, Manini S, Izzo R. VMTK, the Vascular Modeling Toolkit; 2004–2018. http://www.vmtk.org/.

[39] Geronzi L, Gasparotti E, Capellini K, Cella U, Groth C, Porziani S, et al. High Fidelity Fluid-Structure Interaction by Radial Basis Functions Mesh Adaption of Moving Walls: A Workflow Applied to an Aortic Valve. Journal of Computational Science. 2021;51:101327. Available from: https://www.sciencedirect.com/science/article/pii/S1877750321000259.

[40] Hoeijmakers MJMM, Morgenthaler V, Rutten MCM, van de Vosse FN. Scale-Resolving Simulations of Steady and Pulsatile Flow Through Healthy and Stenotic Heart Valves. Journal of Biomechanical Engineering. 2021 11;144(3). 031010. Available from: https://doi.org/10.1115/1.4052459.

[41] De Chant LJ. The Venerable 1/7th Power Law Turbulent Velocity Profile: A Classical Nonlinear Boundary Value Problem Solution and Its Relationship to Stochastic Processes. Appl Math Comput. 2005 feb;161(2):463–474. Available from: https://doi.org/10.1016/j.amc.2003.12.109.

[42] van Ooij P, Farag ES, Blanken CPS, Nederveen AJ, Groenink M, Planken RN, et al. Fully Quantitative Mapping of Abnormal Aortic Velocity and Wall Shear Stress Direction in Patients with Bicuspid Aortic Valves and Repaired Coarctation Using 4D Flow Cardiovascular Magnetic Resonance. Journal of Cardiovascular Magnetic Resonance. 2021 Dec;23(1):9. Available from: https://jcmr-online.biomedcentral.com/articles/10.1186/s12968-020-00703-2.

[43] Garcia J, van der Palen RLF, Bollache E, Jarvis K, Rose MJ, Barker AJ, et al. Distribution of Blood Flow Velocity in the Normal Aorta: Effect of Age and Gender. Journal of Magnetic Resonance Imaging. 2018 Feb;47(2):487-98. Available from: https://onlinelibrary.wiley.com/doi/10.1002/jmri.25773.

[44] Richards CE, Parker AE, Alfuhied A, McCann GP, Singh A. The Role of 4-Dimensional Flow in the Assessment of Bicuspid Aortic Valve and its Valvulo-Aortopathies. The British Journal of Radiology. 2022 Nov;95(1139):20220123. Available from: https://www.birpublications.org/doi/10.1259/bjr.20220123.

[45] Alastruey J, Passerini T, Formaggia L, Peiró J. Physical Determining Factors of the Arterial Pulse Waveform: Theoretical Analysis and Calculation Using the 1-D Formulation. Journal of Engineering Mathematics. 2012 Dec;77(1):19-37. Available from: http://link.springer.com/10.1007/s10665-012-9555-z.

[46] Feher J. Multiscale, Multiphysics and Reduced Order Modelling Techniques for Hemodynamics [Ph.D. thesis]. Politecnico di Milano; 2019. Available from: https://www.politesi.polimi.it/handle/10589/150631.

[47] Lilly DK. A Proposed Modification of the Germano Subgrid-Scale Closure Method. Physics of Fluids A: Fluid Dynamics. 1992;4(3):633-5. Available from: https://doi.org/10.1063/1.858280.

[48] Cho YI, Kensey KR. Effects of the Non-Newtonian Viscosity of Blood on Flows in a Diseased Arterial Vessel. Part 1: Steady flows. Biorheology. 1991 Jun;28(3-4):241-62. Available from: https://www.medra.org/servlet/aliasResolver?alias=iospress&doi=10.3233/BIR-1991-283-415.

[49] Johnston BM, Johnston PR, Corney S, Kilpatrick D. Non-Newtonian Blood Flow in Human Right Coronary Arteries: Steady State Simulations. Journal of Biomechanics. 2004;37(5):709-20. Available from: https://www.sciencedirect.com/science/article/

pii/S0021929003003579.

[50] Weddell JC, Kwack J, Imoukhuede PI, Masud A. Hemodynamic Analysis in an Idealized Artery Tree: Differences in Wall Shear Stress between Newtonian and Non-Newtonian Blood Models. PLOS ONE. 2015 Apr;10(4):e0124575. Available from: https://dx.plos.org/10.1371/journal.pone.0124575.

[51] Iasiello M, Vafai K, Andreozzi A, Bianco N. Analysis of Non-Newtonian Effects on Low-Density Lipoprotein Accumulation in an Artery. Journal of Biomechanics. 2016 Jun;49(9):1437-46. Available from: https://linkinghub.elsevier.com/retrieve/pii/S0021929016303086.

[52] Arzani A. Accounting for Residence-Time in Blood Rheology Models: Do We Really Need Non-Newtonian Blood Flow Modelling in Large Arteries? Journal of The Royal Society Interface. 2018;15(146):20180486. Available from: https://royalsocietypublishing.org/doi/abs/10.1098/rsif.2018.0486.

[53] Morbiducci U, Ponzini R, Gallo D, Bignardi C, Rizzo G. Inflow Boundary Conditions for Image-Based Computational Hemodynamics: Impact of Idealized Versus Measured Velocity Profiles in the Human Aorta. Journal of Biomechanics. 2013;46(1):102-9. Available from: https://www.sciencedirect.com/science/article/pii/S0021929012006100.

[54] Mendez V, Di Giuseppe M, Pasta S. Comparison of Hemodynamic and Structural Indices of Ascending Thoracic Aortic Aneurysm as Predicted by 2-way FSI, CFD Rigid Wall Simulation and Patient-Specific Displacement-Based FEA. Computers in Biology and Medicine. 2018 Sep;100:221-9. Available from: https://linkinghub.elsevier.com/retrieve/pii/S001048251830204X.

(1) Non-Newtonian viscosity has greater impact on WSS than LES turbulence modelling.

(2) Non-Newtonian effects are amplified when incorporating a LES model

(3) Wall shear stress is underestimated when considering Newtonian viscosity 2.9-5.0%.

(4) A minimum of 15 cycles should be performed when assessing computational methods.

Declaration of Interest Statement

Authors AM, MH, LG, VM and MR were employed by Ansys France. The remaining authors declare that the research was conducted in the absence of any commercial or financial relationships that could be construed as a potential conflict of interest.